

ADVANCED MATERIALS

Supporting Information

for *Adv. Mater.*, DOI 10.1002/adma.202308353

Pseudopolymorphic Phase Engineering for Improved Thermoelectric Performance in Copper Sulfides

Tian-Yu Yang, Shi-Wei Gu, Yi-Xin Zhang, Fengshan Zheng, Deli Kong, Rafal E. Dunin-Borkowski, Di Wu, Zhen-Hua Ge, Jing Feng* and Lei Jin**

Supporting Information

Pseudopolymorphic Phase Engineering for Improved Thermoelectric Performance in Copper Sulfides

Tian-Yu Yang, Shi-Wei Gu, Yi-Xin Zhang, Fengshan Zheng, Deli Kong, Rafal E. Dunin-Borkowski, Di Wu, Zhen-Hua Ge, Jing Feng*, and Lei Jin**

Electron probe X-ray micro-area analysis (EPMA)

The copper-sulfur ratio was investigated using electron probe X-ray micro-area analysis testing. Figure S1 shows EPMA results for the best performing samples, revealing mass ratios for Cu and S of 71.8% and 28.2%, respectively.

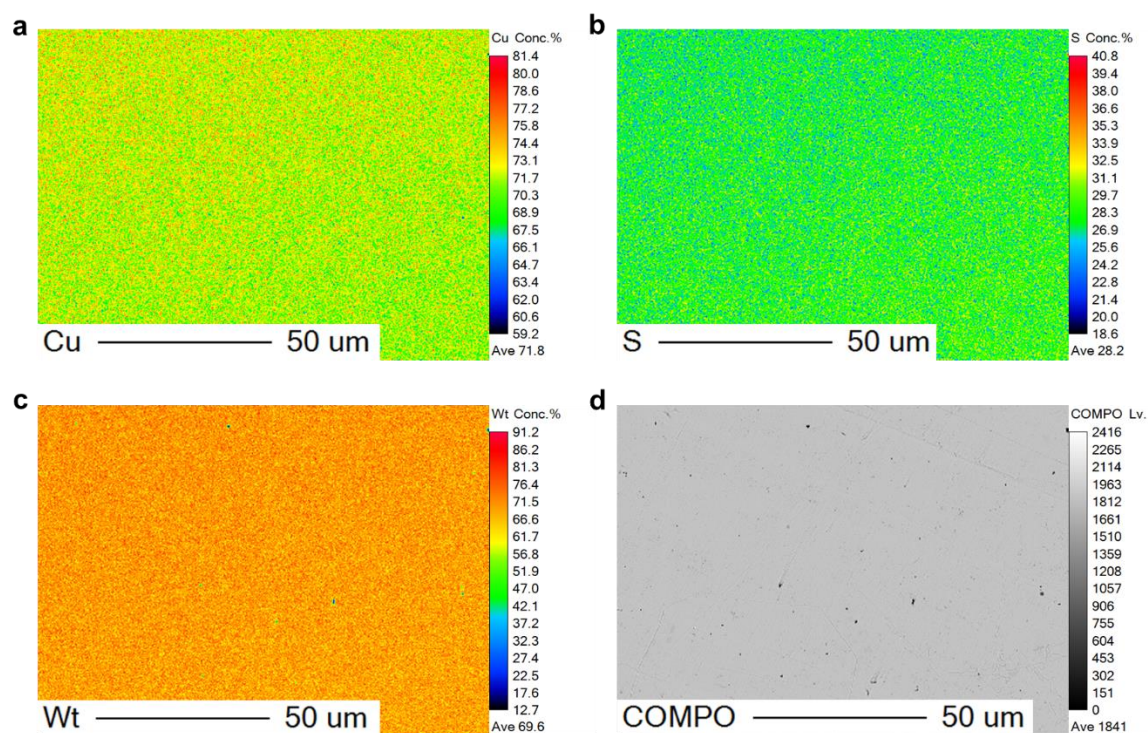


Figure S1. a-d Surface distribution of sample surface microregions scanned using EPMA.

Five points were selected for point scanning of the sample area and atomic ratio analysis, as shown in Figure S2.

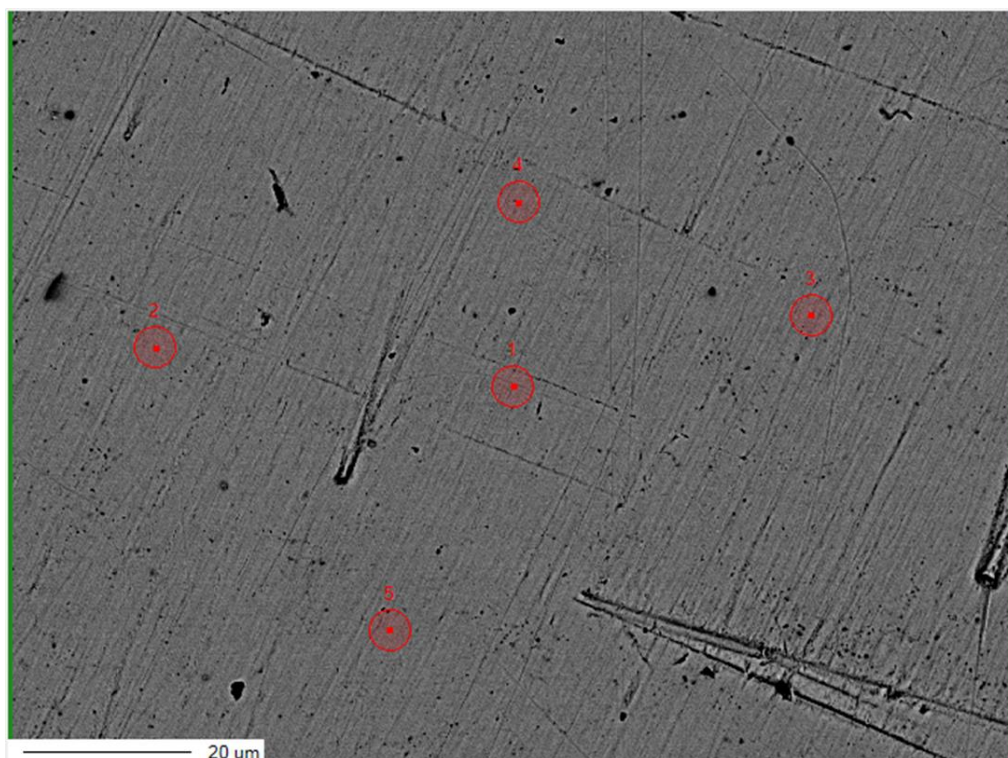


Figure S2. EPMA point scanning area diagram.

Table S1 shows that the Cu-S atomic ratio of the sample measured from the point scans is similar to that of intrinsic $\text{Cu}_{1.8}\text{S}$, suggesting that the sample is $\text{Cu}_{1.8}\text{S}$ and that no transformations of sample properties have occurred.

Table S1. Atomic ratio data obtained in EPMA point scanning mode.

	1	2	3	4	5	Ave.	$\text{Cu}_{1.8}\text{S}$
Cu	64.0372	64.1414	63.9938	64.0226	64.0208	64.0432	64.2857
S	35.9628	35.8586	36.0062	35.9774	35.9792	35.9568	35.7143
Cu/S	1.7807	1.7887	1.7773	1.7795	1.7794	1.7811	1.8

Intergrowth of monoclinic and hexagonal phase

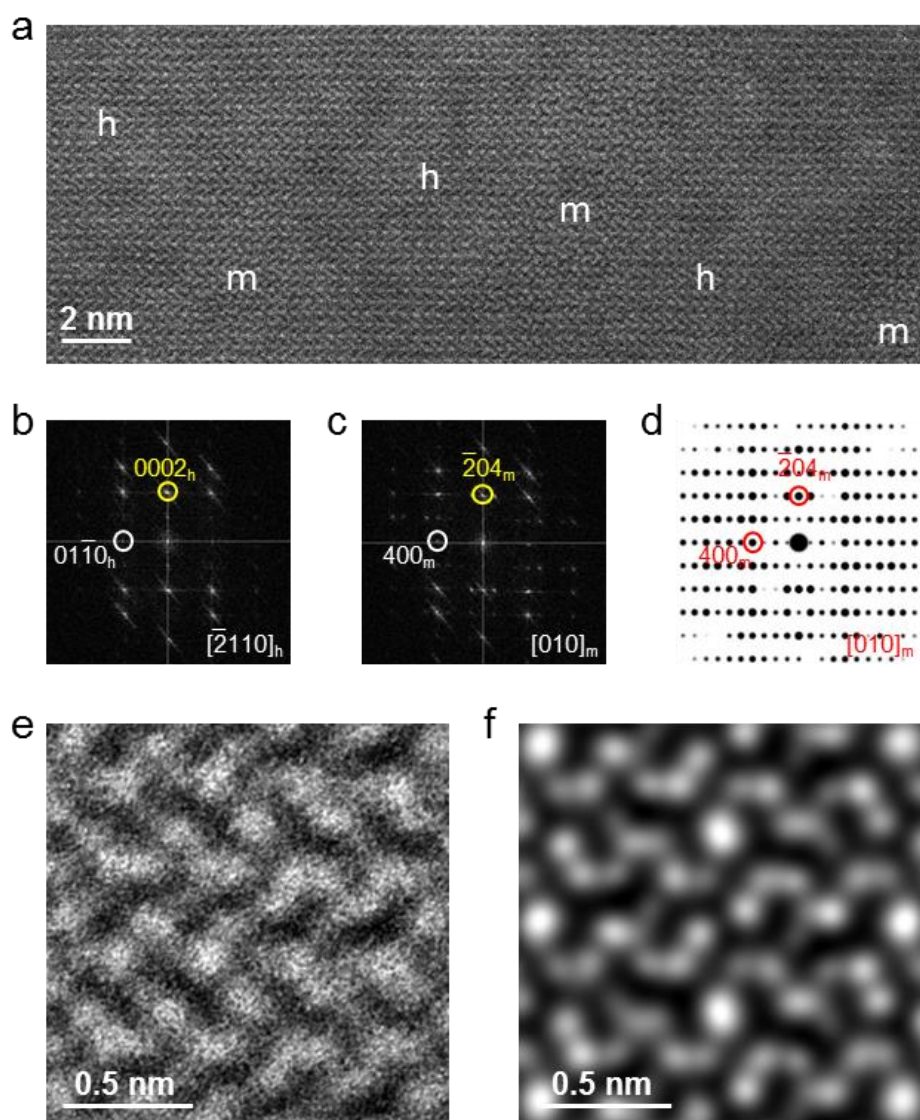


Figure S3. Atomic-resolution high-angle annular dark-field (HAADF) scanning transmission electron microscopy (STEM) images and corresponding fast Fourier transforms (FFTs). **a** HAADF STEM image showing an intergrowth of monoclinic (m) and hexagonal (h) phases at room temperature (RT). **b** FFT from the h phase. **c** FFT from the m phase. **d** Simulated electron diffraction pattern of the m phase based on kinematical electron diffraction theory. **e** Averaged experimental HAADF image of the m phase shown in **a**. **f** Corresponding simulated image created from a model of Cu_2S (ICSD 100333). The orientation relationship between the two phases is $(\bar{2}04)_m \parallel (0002)_h$, $(400)_m \parallel (01\bar{1}0)_h$ and $[010]_m \parallel [\bar{2}110]_h$.

In situ X-ray diffraction (XRD)

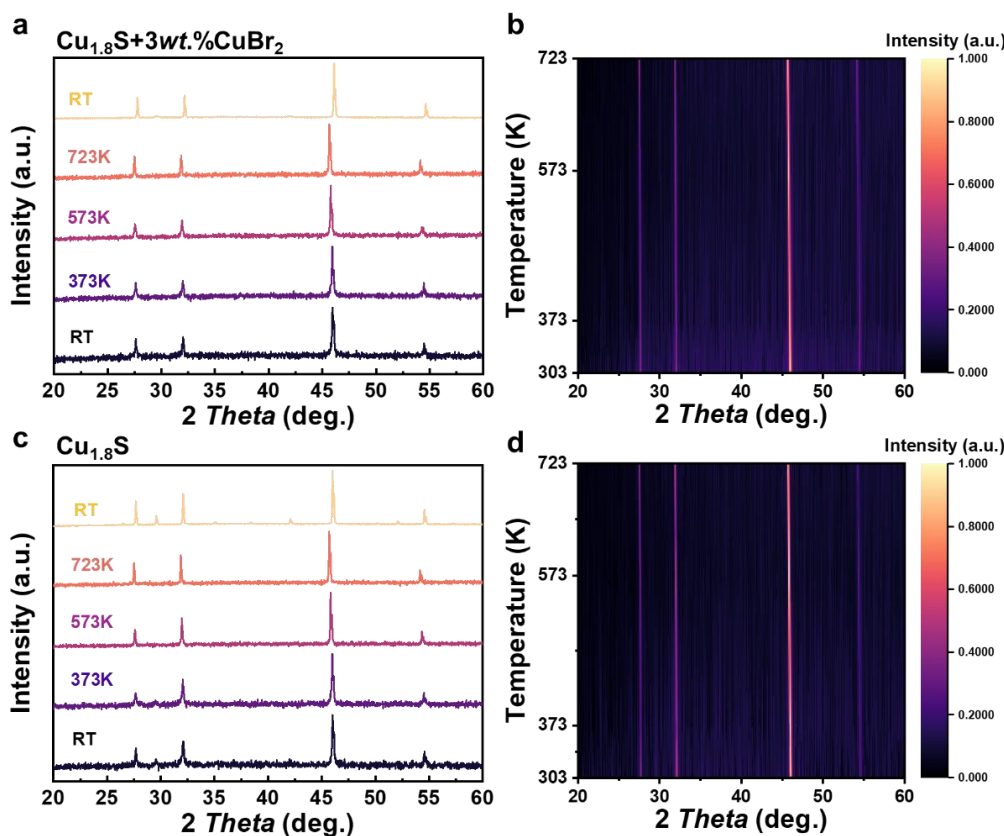


Figure S4. Temperature-dependent XRD patterns from RT to 723 K for Cu_{1.8}S and the 3 wt.% CuBr₂ doped sample. **a** XRD patterns for the Cu_{1.8}S + 3 wt.% CuBr₂ sample. **b** Temperature-dependent 2D Guinier pattern for the Cu_{1.8}S + 3 wt.% CuBr₂ sample. **c** XRD patterns for pure Cu_{1.8}S. **d** Temperature-dependent 2D Guinier pattern for pure Cu_{1.8}S.

We performed in situ XRD (Bruker D8, Germany) from RT to 723 K to understand the PP-engineered phase stability. The results are shown in Figure S4. Over the entire temperature range, the 3 wt.% CuBr₂ doped sample exhibits a 1*a* cubic matrix phase (RT – high temperature (HT) – RT), while the pure sample undergoes a 6*a* – 1*a* – 6*a* transition (RT – HT – RT), as reported in the literature. No other secondary phase is seen. These results support our argument that the PP-engineered 1*a* matrix phase is thermodynamically stable. No reversible transition

back to the pristine $6a$ phase is detected. The $1a$ matrix phase can therefore be used as a new platform for further broadening the range of working temperature and/ or improving the thermoelectric performance of $\text{Cu}_{1.8}\text{S}$ to the temperature applied.

In situ 4D-STEM

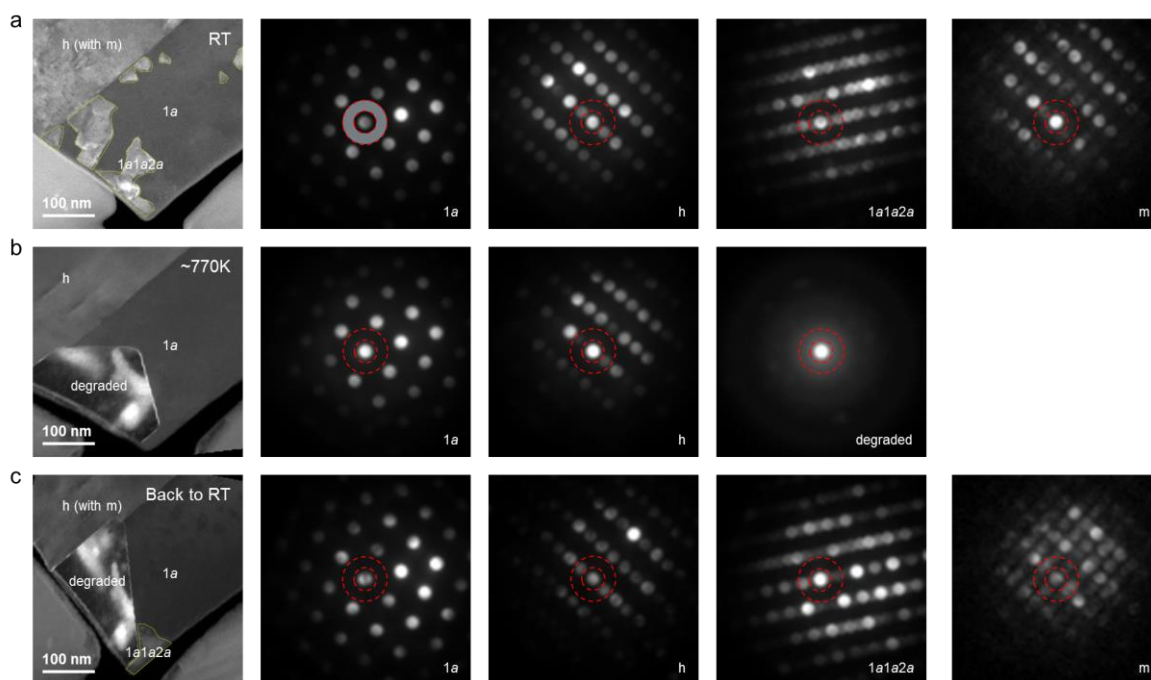


Figure S5. Left panel: reconstructed real space images. Other panels: representative diffraction patterns recorded from the pseudopolymorphic phases, extracted from 4D-STEM datasets. The semi-convergence angle is ~ 1.7 mrad and the probe size is ~ 2 nm.

Results of in situ 4D-STEM investigations are shown in Figure S5. A nanometer-sized electron probe was scanned across the sample area (*i.e.*, 2D real space). At each scan position, an electron diffraction pattern (*i.e.*, 2D reciprocal space) was recorded using a fast camera, thereby forming a 4D dataset. The results allow the phase distribution and corresponding orientation relationships to be studied over a large field of view. The left panel in Figure S5 shows real space images reconstructed from the diffraction intensities summed over the annular areas

marked by red dashes. The other panels show representative diffraction patterns recorded from the pseudopolymorphic phases. Both the $1a$ matrix phase and the Cu_2S hexagonal (h) phase can be maintained up to ~ 770 K (limited by the heating instrument in our microscope) and the associated interface is robust. The m phase is no longer detected at 450 K, while the $1a1a2a$ phase vanishes between 450 and 570 K (not shown), suggesting that both phases have a limited contribution to the peak value of ZT . Nevertheless, it may be beneficial to broaden the applicable temperature range of PPE $\text{Cu}_{1.8}\text{S}$ at intermediate temperatures. The $m - h - m$ and $1a1a2a - 1a - 1a1a2a$ (RT – HT – RT) transitions are reversible and are therefore most likely to be polymorphic phase transitions.

Room temperature Hall results

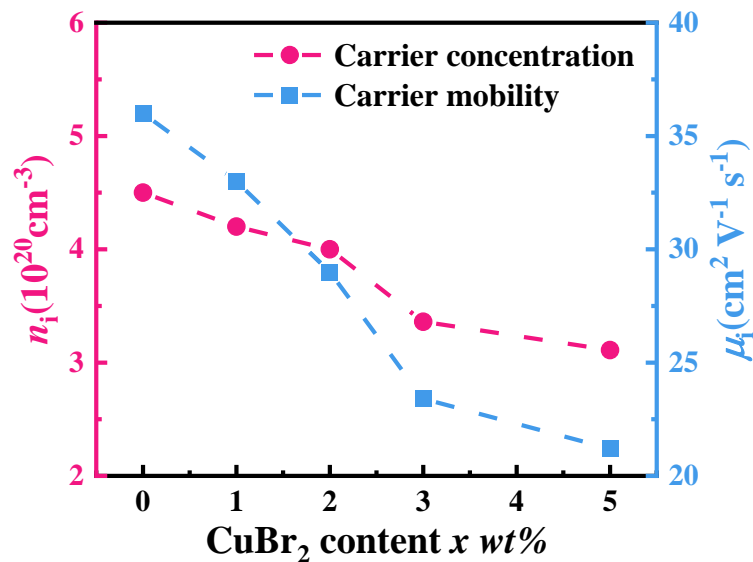


Figure S6. Room temperature carrier concentration n_i and mobility μ_i plotted as a function of CuBr_2 content.

Figure S6 shows the variation in carrier concentration and mobility with CuBr_2 content at room temperature. As additional electrons are introduced, excess electrons and holes annihilate, leading to a reduction in carrier concentration.

Morphology of bulk $\text{Cu}_{1.8}\text{S}$ with different CuBr_2 contents

The microstructure of the $\text{Cu}_{1.8}\text{S} + x \text{ wt.}\% \text{ CuBr}_2$ ($x = 0, 1, 2, 3, 5$) bulk samples was studied using field emission scanning electron microscopy, as shown in Figure S7. Figure S7a shows the micromorphology of the pristine $\text{Cu}_{1.8}\text{S}$ sample. The grain size of the pristine sample is approximately $1 \mu\text{m}$. Figure S7b-S7e shows that the grain size increases gradually as the CuBr_2 content is increased, reaching $5 \mu\text{m}$ when the doping amount is $5 \text{ wt.}\%$. With the introduction of CuBr_2 , the cross-sectional morphology of the specimen gradually evolves from the initial appearance of pores at grain edges to the appearance of pores on the grain surface. This change is likely to occur because the low melting point ($498 \text{ }^\circ\text{C}$) of CuBr_2 acts as a sintering aid during SPS to promote grain growth, with intergranular fracture eventually occurring in the most highly doped $\text{Cu}_{1.8}\text{S} + 5 \text{ wt.}\% \text{ CuBr}_2$ sample, resulting in the formation of additional pores on the grain surface. Figure S7f shows that the increased number of pores results in a decrease in sample density. The advantage is that the pores can be regarded as a thermally insulating phase, which does not have the ability to transport hole carriers and effectively reduces carrier mobility. In this way, the pores act as an effective thermal barrier component, slowing down the rate of phonon transport and decreasing the lattice thermal conductivity of the copper sulfide materials.

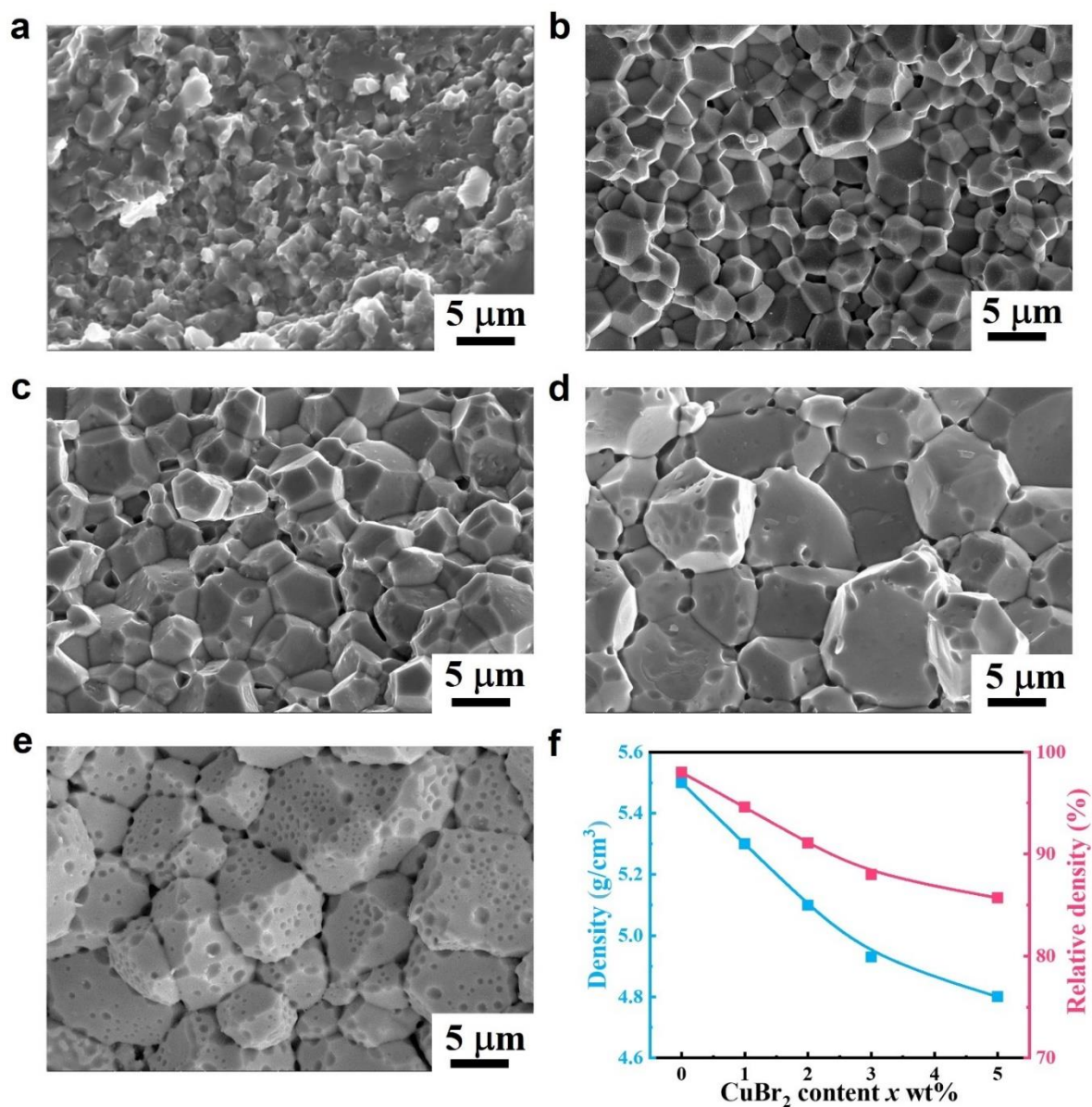


Figure S7. Scanning electron micrographs of bulk $\text{Cu}_{1.8}\text{S}$ with different CuBr_2 contents. **a** Pristine $\text{Cu}_{1.8}\text{S}$; **b** $\text{Cu}_{1.8}\text{S} + 1$ wt.% CuBr_2 ; **c** $\text{Cu}_{1.8}\text{S} + 2$ wt.% CuBr_2 ; **d** $\text{Cu}_{1.8}\text{S} + 3$ wt.% CuBr_2 ; **e** $\text{Cu}_{1.8}\text{S} + 5$ wt.% CuBr_2 . **f** Density/ relative density in the $\text{Cu}_{1.8}\text{S} + x$ wt.% CuBr_2 ($x = 0, 1, 2, 3, 5$) samples.

Thermal conductivity

In a previous study, the lattice thermal conductivity of $\text{Cu}_{1.8}\text{S}$ was examined.^[1] In this study, it was proposed that the Wiedemann-Franz equation $\kappa_e = L\sigma T$ (where κ_e , L , σ , T are the carrier thermal conductivity, Lorentz constant, electrical conductivity and absolute temperature, respectively) may not be suitable for Cu_9S_5 superionic conductors due to the distinct thermal transport properties of electron/ hole carriers and ion carriers. There are currently challenges in measuring ionic conductivity and ion thermal conductivity in the copper sulfide system. If the ionic conductivity (σ_i) and ion thermal conductivity (κ_i) can be measured, then the carrier thermal conductivity can be calculated by using the modified equation $\kappa_e = L(\sigma - \sigma_i)T + \kappa_i$. By building on the aforementioned theory and previous studies^[2], we developed a method for calculating the modified Lorentz constant. We used the literature-reported lattice thermal conductivity to deduce the electron thermal conductivity and obtained a new Lorentz constant. We compared the new Lorentz constant with that of the SPB model to determine the difference between them. This difference can be defined as the Lorentz constant contribution from Cu ions, which we refer to as Δ_i . The modified Lorentz constant can be calculated by using the equation $L_m = L + \Delta_i$, where L_m , L and Δ_i are the modified Lorentz constant, the Lorentz constant and the difference in the value between the SPB model and the calculated Lorentz constant, respectively. The Lorentz constant equation calculated by the reduced Fermi level takes the form

$$L = \left(\frac{k_B}{e}\right)^2 \left(\frac{(\gamma+7/2)F_{\gamma+5/2}(\eta)}{(\gamma+3/2)F_{\gamma+1/2}(\eta)} - \left[\frac{(\gamma+5/2)F_{\gamma+3/2}(\eta)}{(\gamma+3/2)F_{\gamma+1/2}(\eta)} \right]^2 \right). \quad (1)$$

The Lorentz constant mentioned above was estimated using a traditional single parabolic band model, which resulted in an L value with a deviation of less than 10% when compared with more rigorous calculations using a single non-parabolic band and multiple band models.^[3-5] This approach allowed us to derive the modified Lorentz constant and to calculate the electron thermal conductivity and lattice thermal conductivity from it, as shown in Figure S8.

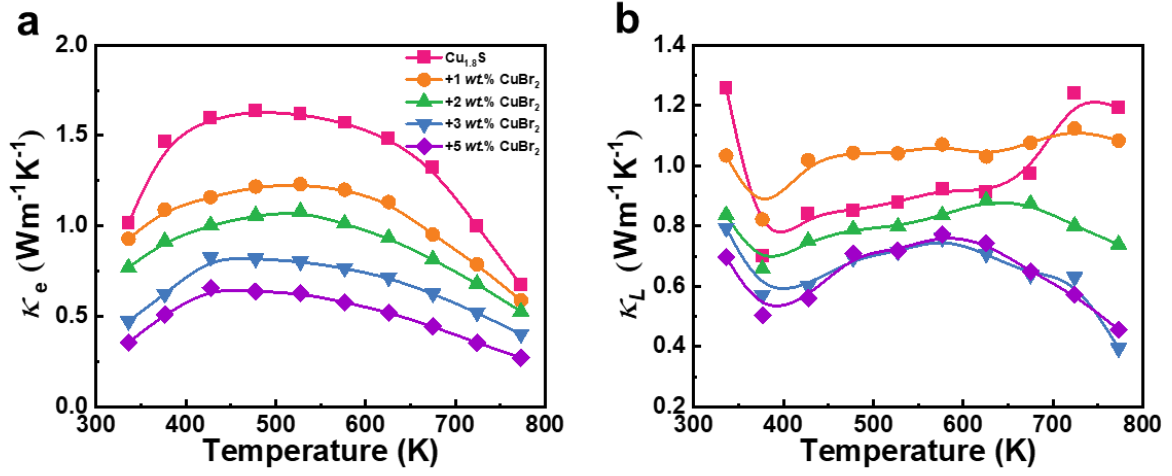


Figure S8. **a** Carrier thermal conductivity κ_e and **b** lattice thermal conductivity κ_l plotted as a function of temperature.

Lattice thermal conductivity prediction using the Debye-Callaway model

In order to further establish the relationship between PPE and high thermoelectric performance, the lattice thermal conductivity was fitted using the Debye-Callaway model.^[6] Theoretically, the lattice thermal conductivity κ_l can be calculated from the equation

$$\kappa_l = \frac{k_B}{2\pi^2 v_s} \left(\frac{k_B T}{\hbar} \right) \int_0^{\theta_D} \tau_{\text{tot}} \frac{z^4 e^z}{(e^z - 1)^2} dz \quad (\text{S1})$$

where k_B is the Boltzmann constant, v_s is the average speed of sound, \hbar is the reduced Planck constant, θ_D is the Debye temperature, $z = \hbar\omega/k_B T$ (where ω is the phonon frequency) is the reduced phonon frequency and τ_{tot} is the total relaxation time.

The integrand, in conjunction with the coefficient in Equation S1, describes the spectral lattice thermal conductivity (κ_s), where

$$\kappa_s = \frac{k_B}{2\pi^2 v_s} \left(\frac{k_B T}{\hbar} \right)^3 \tau_{\text{tot}} \frac{z^4 e^z}{(e^z - 1)^2} \quad (\text{S2})$$

$$\tau_{\text{tot}}^{-1} = \tau_{\text{U}}^{-1} + \tau_{\text{GB}}^{-1} + \tau_{\text{PD}}^{-1} + \tau_{\text{PB}}^{-1} + \tau_{\text{D}}^{-1} + \tau_{\text{NP}}^{-1} \quad (\text{S3})$$

Umklapp scattering process:

$$\tau_{\text{U}}^{-1} = \frac{\hbar\gamma^2}{Mv_s^2\theta_{\text{D}}} \omega^2 T \exp\left(-\frac{\theta_{\text{D}}}{3T}\right) \quad (\text{S4})$$

Normal process:

$$\tau_{\text{N}}^{-1} = \beta\tau_{\text{U}}^{-1} \quad (\text{S5})$$

Grain boundary scattering:

$$\tau_{\text{GB}}^{-1} = \frac{v_s}{d} \quad (\text{S6})$$

Point defect scattering:

$$\tau_{\text{PD}}^{-1} = \frac{\bar{V}\omega^4}{4\pi v_s^3} \Gamma \quad (\text{S7})$$

Phase boundary scattering:

$$\tau_{\text{PB}}^{-1} = A \frac{v_s}{d_{\text{PB}}} \quad (\text{S8})$$

Dislocation scattering:

$$\tau_{\text{D}}^{-1} = \tau_{\text{DC}}^{-1} + \tau_{\text{DS}}^{-1} \quad (\text{S9})$$

$$\tau_{\text{DC}}^{-1} = N_{\text{D}} \frac{\bar{V}^{4/3}}{v_s^2} \omega^3 \quad (\text{S10})$$

$$\tau_{\text{DS}}^{-1} = 0.6 B_{\text{D}}^2 N_{\text{D}} \gamma^2 \omega \left[\frac{1}{2} + \frac{1}{24} \left(\frac{1-2r}{1-r} \right) \left(1 + \sqrt{2} \left(\frac{v_1}{v_t} \right)^2 \right) \right] \quad (\text{S11})$$

Nanoprecipitate scattering:

$$\tau_{\text{NP}}^{-1} = V(\sigma_s^{-1} + \sigma_1^{-1})^{-1} V_{\text{NP}} \quad (\text{S12})$$

$$\sigma_s = 2\pi R^2 \quad (\text{S13})$$

$$\sigma_1 = \pi R^2 \frac{4}{9} \left(\frac{\Delta D}{D_{\text{m}}} \right)^2 \left(\frac{\omega R}{v_s} \right)^4 \quad (\text{S14})$$

The parameters used for phonon modeling are listed in Table S2. A further result is shown in Figure S9.

Table S2. Parameters for phonon modeling of the Cu_{1.8}S + 3 wt.% CuBr₂ sample

Parameters	Symbols	Values
Debye temperature	θ_D (K)	232
Additional factor for integrating τ_U and τ_N	β	2.5
Longitudinal sound velocity	v_l (m/s)	3825.78
Transverse sound velocity	v_t (m/s)	1582.35
Sound velocity	v_s (m/s)	2330.16
Average atomic mass	\bar{M} (kg)	1.65×10^{-25}
Average atomic volume	\bar{V} (m ³)	2×10^{-29}
Dislocation density	N_D (cm ⁻²)	4×10^{15}
Average grain size	d (μ m)	10
Alloy scattering factor	Γ	0.2
Burgers vector	B_D (nm)	1.2
Average radius of nanoprecipitates	R [μ m]	3
Mass density of matrix	D_m [kg/m ³]	6000
Mass density of nano precipitates	D_{NP} [kg/m ³]	4000
Number density of nanoprecipitates	V_{NP} (cm ⁻³)	4×10^{15}
Poisson's ratio	r	0.4
Grüneisen parameter	γ	2.2
Phase boundary width	d_{PB} (nm)	110
Phase boundary fitting parameter	A	0.1

Figure S9a shows that κ_l is reduced gradually *via* PPE in the CuBr_2 -modified samples. The solid orange line indicates the contribution from Umklapp scattering, grain boundary scattering and point defect scattering. The arrows represent the contribution of phase boundary scattering to phonon transport, indicating that phase boundaries introduced by PPE play an important role in decreasing the lattice thermal conductivity. The frequency-dependent cumulative reduction in κ_l is presented in Figure S9b. Grain boundaries are responsible for scattering low-frequency phonons, while point defects target high-frequency phonons. Phase boundaries, dislocations and nanoprecipitates effectively reduce κ_l by scattering mid-frequency phonons. Consequently, phonon transport behavior is suppressed by (pseudo-)polymorphic phases and (semi-)coherent phase boundaries *via* PPE.

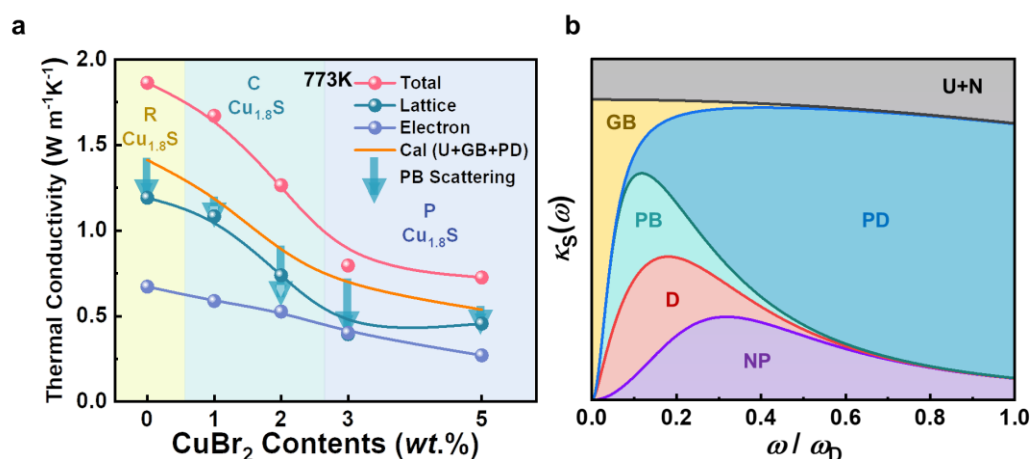


Figure S9. Lattice thermal conductivity κ_l and Debye-Callaway model prediction. **a** CuBr_2 -content-dependent thermal conductivity at 773 K. **b** Calculated lattice thermal conductivity using the Debye-Callaway model with different scattering mechanisms including Umklapp scattering (U), grain boundary scattering (GB), point defect scattering (PD), phase boundary scattering (PB), dislocation scattering (D) and nanoprecipitate scattering (NP) at 300 K.

Note 1: Difference between PPE and polymorphic phase boundaries (PPBs) in piezoelectric materials

Polymorphic phase boundaries (PPBs) in piezoelectric materials, most of which have perovskite ABO_3 structures, delimit temperature and/ or pressure driven phase transitions, in which both intrinsic and extrinsic contributions are maximized, thereby enhancing the macroscopic properties of piezoelectricity.^[7] Another concept is referred to as morphotropic phase boundaries (MPBs) in piezoelectric materials. Similar to PPE, this concept describes a phase transition driven by composition.^[6] In PPB and MPB, the engineered phases usually have the same perovskite structure, but exhibit different lattice distortions (*e.g.*, with rhombohedral, orthorhombic and tetragonal distortions). The variation in lattice distortion can change the electrostatic energy by locally forming ferroelectric phases and changing the elastic energy of the system through internal strain, leading to an improvement in piezoelectric performance. In contrast to PPB and MPB, PPE in the present study is more general and does not require strict structural similarity between the constituent phases.

Note 2: Prospective application of PPE

The best thermoelectric performance of materials such as $Cu_{1.8}S$ and $SnSe$ is often achieved at an elevated temperature, before/ at which the structural phase transition occurs. The structure that is responsible for thermoelectric performance is usually not the structure that is crystallographically stable at RT. For example, in addition to $Cu_{1.8}S$ (exhibiting a $6a$ to $1a$ transition at ~ 360 K, as discussed in the main text), $SnSe$ undergoes a RT $Pnma$ to HT $Cmcm$ transition (~ 800 K), which is found to be the origin of its superior thermoelectric performance.^[8] Stabilization of the metastable HT phase (usually with better thermoelectric

performance) down to RT can offer a better platform for further broadening the range of working temperature and/ or improving thermoelectric performance to the temperature applied. This is a core consideration for PPE. Similar attempts have recently been reported for SnSe by modification of GaSe.^[9,10]

PPE is also expected to be relevant for other thermoelectric properties that exhibit phase transitions during heating, for example in Cu₂Se, GeTe and Cu₁₂Sb₄S₁₃. Obtaining the HT phase at RT for thermoelectric materials may result in a further benefit by removing the phase transition point during heating and avoiding a volume change that may cause device failure.

References

- [1] Z.-H. Ge, X. Liu, D. Fen, J. Lin, J. He, *Adv. Energy Mater.* **2016**, *6*, 1600607.
- [2] Z.-H. Ge, X. Chong, D. Feng, Y.-X. Zhang, Y. Qiu, L. Xie, P.-W. Guan, J. Feng, J. He, *Mater. Today Phys.* **2019**, *8*, 71.
- [3] M.-L. Liu, F.-Q. Huang, L.-D. Chen, L.-W. Chen, *Appl. Phys. Letter.* **2009**, *94*, 202103.
- [4] L.D. Zhao, B.-P. Zhang, J.-F. Li, H.L. Zhang, W.S. Liu, *Solid State Sci.* **2008**, *10*, 651.
- [5] D.P. White, P.G. Clemens, *J. Appl. Phys.* **1992**, *71*(9), 4258.
- [6] J. Callaway, *Phys. Rev.* **1959**, *113*, 1046-1051.
- [7] J.E. Garcia, F. Rubio-Marcos, *J. Appl. Phys.* **2020**, *127*, 131102.
- [8] L.-D. Zhao, S.-H. Lo, Y. Zhang, H. Sun, G. Tan, C. Uher, C. Wolverton, V.P. Dravid, M.G. Kanatzidis, *Nature* **2014**, *508*, 373-377.
- [9] B.E. Matthews, A.M. Holder, L.T. Schelhas, S. Siol, J.W. May, M.R. Forkner, D. Vigil-Fowler, M.F. Toney, J.D. Perkins, B.P. Gorman, A. Zakutayev, S. Lany, J. Tate, *J. Mater. Chem. A* **2017**, *5*, 16873-16882.
- [10] S.-K. Cha, S. Im, Y.-S. Kim, *ACS Appl. Energy Mater.* **2022**, *5*, 2067-2073.